NON-HOMOGENEOUS BOUNDARY CONDITIONS AND CAVITATION MODELING FOR REYNOLDS EQUATION

Alfredo Jaramillo[a]**, Hugo M. Checo**[a] **and Gustavo C. Buscaglia**[a]

[a]*Inst. de Ciências Matemáticas e de Computação, Universidade de São Paulo, 13560-970 São Carlos, Brazil, http://www.icmc.usp.br*

Keywords: Surface-texturing, cavitation modeling, Elrod-Adams model, back-pressure effects.

Abstract. When simulating numerically the hydrodynamical lubrication of tribological devices, a common assumption is that the boundary pressure and the cavitation pressure are equal (and taken equal to zero). This allows to include cavitation effects through some of the available algorithms, like the mass-conserving Elrod-Adams cavitation model. However, tribological devices often work under non-homogeneous pressure conditions. An example of this is the cylinder/piston-rings system, where the pressure difference between both sides of the ring reach levels in the order of 50 atm during compression and ignition. In this work we propose an extension of the Elrod-Adams model in order to accommodate such non-homogeneous pressure conditions by assuming a dependence of the algorithmic cavitation pressure on the saturation variable. A first algorithm for solving the resulting model is proposed. Also, preliminary tests results on how the back-pressure may affect the dynamics of the rings during the compression/power stroke are reported.
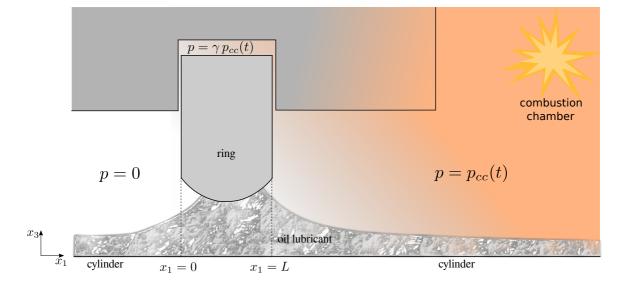
1   INTRODUCTION

Several factors must be considered when modeling the piston ring/cylinder liner (PRCL) system. Developed forces, surface textures and pressure boundary conditions are among those factors doing such modeling a challenging problem. During the compression stroke, the combustion chamber pressure achieve values as high as 60 atm, which may have important consequences on the rings dynamic.

Divergent geometry and squeeze motion may produce tensile stresses (negative pressures) that can lead to a local rupture of the fluid film, which is known as cavitation. Several non-connected cavitated regions can appear when including surface textures. In that case, as proved by Ausas et al. (2007), to obtain accurate results it is essential to use a mass conservative model like the Elrod-Adams cavitation model.

Experimental and numerical findings have shown that surface texturing can have beneficial or detrimental effects depending on geometrical parameters, like texture defining parameters and ring profiles, and the Stribeck number (*speed × viscosity / applied load*) (Kovalchenko et al., 2004; Etsion, 2005; Tomanik, 2008; Dobrica et al., 2010; Gadeschi et al., 2012; Checo et al., 2014). However, when studying the PRCL system, the majority of the studies do not take into account the tribological response of that system to the highly variable combustion chamber pressure. And the few that has been published use a non-conservative algorithm (Morris et al., 2014, 2015; Usman and Park, 2016).

In this paper, a first step to extend the Elrod-Adams model is made. Such extension models the effects of the combustion chamber pressure and cavitation along a mass-conservative algorithm. Such extension applies a constrain on the hydrodynamical pressure depending on the saturation variable.

This work is organized as follows: The details of the mathematical modeling are presented in Section 2. In Section 3 the discrete model and the numerical algorithm proposed are presented. In Section 4 the results of first numerical test are shown. Finally, in Section 5 some conclusions and future research are presented.

2   MATHEMATICAL MODELING

Figure 1: 1-D physical scheme of the simulations. The computational domain is $\Omega = [0, L]$.

A 1-D physical scheme of the simulations is shown in Fig. 1. Consider the domain (the region just under the ring) $\Omega = [0, L] \times [0, B]$ and denote its boundary by Γ, with sides $\Gamma_\ell = \{(0, x_2), x_2 \in [0, B]\}$, $\Gamma_r = \{(1, x_2), x_2 \in [0, B]\}$, the left and right sides respectively, being U the relative velocity between the surfaces. The unknowns of the problem are: the hydrodynamic pressure $p(x_1, x_2, t)$, the saturation variable $\theta(x_1, x_2, t)$ and the cavitation pressure $p_{cav}(x_1, x_2, t)$.

The Elrod-Adams model incorporates into a single formulation the Reynolds equation and the Jacobson-Floberg-Olsson boundary conditions for the rupture and reformation boundaries. We propose an extension of that model, reading

$$\text{div}\left(\frac{h^3}{12\,\mu}\nabla p - \frac{U}{2}h\theta\,\hat{e}_1\right) = \frac{\partial h\theta}{\partial t}, \qquad \text{on } \Omega, \qquad (1)$$

$$p \geq p_{cav},\ 0 \leq \theta \leq 1, \qquad \text{on } \Omega, \qquad (2)$$

$$(p - p_{cav})(1 - \theta) = 0, \qquad \text{on } \Omega, \qquad (3)$$

$$p(0, x_2, t) = p_{cav}(0, x_2, t), \qquad \text{on } \Gamma_\ell, \qquad (4)$$

$$p(1, x_2, t) = p_{cav}(1, x_2, t), \qquad \text{on } \Gamma_r, \qquad (5)$$

$$\theta(x_1, x_2, t) = \theta_{feed}, \qquad \text{on } \Gamma_\ell \text{ if } U > 0,\ \text{or } \Gamma_r \text{ if } U < 0, \qquad (6)$$

where the unitary vector $\hat{e}_1$ is oriented along the relative movement direction. We also impose continuity of the flux function (mass-flux)

$$J(x_1, x_2) = -\frac{h^3}{12\,\mu}\nabla p + \frac{U}{2}h\theta\,\hat{e}_1, \qquad (7)$$

and continuity of the second term of the flux function, i.e., the Couette flux. The cavitation pressure is given by the operator T (for each time t):

$$T:\quad L^\infty(\Omega) \mapsto L^\infty(\Omega)$$
$$\theta \quad \mapsto \quad p_{cav} = T(\theta).$$

Let us denote $\Lambda^t = \{(x_1, x_2) \in \Omega : \theta(x_1, x_2, t) < 1\}$, and by Λ_r^t the union of the connected components of Λ^t such that $\Lambda^t \cap \Gamma_r \neq \emptyset$ (observe that it would happen that $|\Lambda_r^t| = 0$). With this, in the present work T is defined as

$$(T\theta)(x_1, x_2) = \begin{cases} p_{cc}(t) & \text{if } (x_1, x_2) \in \Lambda_r^t \\ 0 & \text{if } (x_1, x_2) \notin \Lambda_r^t \end{cases}. \qquad (8)$$

Figure 2 illustrates the action of the operator T used in the examples exposed in this work.

3 DISCRETIZATION

Let us divide Ω in $N_{x_1} \times N_{x_2}$ cells (using half-cells at the boundaries) and denote by I the set of indexes of the cells corresponding to internal nodes (where the unknowns are placed). A finite volumes scheme for Eq. (1) is used, for this, the x_1 flux component going from node $(i-1, j)$ to node (i, j) can be discretized by

$$-\frac{h^3}{12\mu}\frac{\partial p}{\partial x_1} + \frac{U}{2}h\theta \approx -\frac{1}{12\mu}\frac{(h_{i-1,j}^n)^3 + (h_{i,j}^n)^3}{2}\frac{p_{i,j}^n - p_{i-1,j}^n}{\Delta x_1} + \frac{U}{2}h_{i-1,j}^n\theta_{i-1,j}^n, \qquad (9)$$
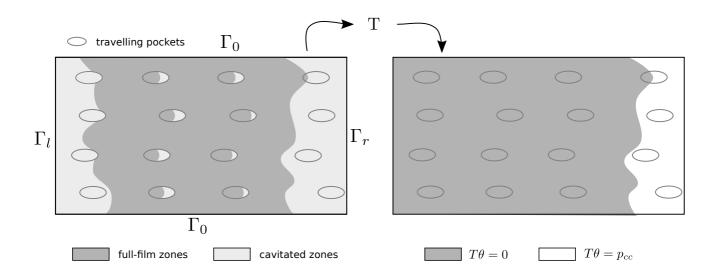
Figure 2: Illustration of the action of the operator T, where θ is the saturation variable and $T\theta$ is the cavitation pressure.

where an upwind scheme is used for the Couette term. Balancing the fluxes on each cell (for the x_2 components only diffusive terms need to be included) and discretizing time along an implicit scheme for the temporal term $\frac{\partial h\theta}{\partial t}$ we get to a system of equations that reads, for each $(i,j) \in I$,

$$a_{i,j}^{00} p_{i,j}^n + e_{i,j}^{00} \theta_{i,j}^n = C_{i,j}(\boldsymbol{p}^n, \boldsymbol{\theta}^n), \tag{10}$$

$$\boldsymbol{p}_{cav}^n = T(\boldsymbol{\theta}), \tag{11}$$

$$p_{i,j}^n \geq p_{cav;i,j}^n, \tag{12}$$

$$0 \leq \theta_{i,j}^n \leq 1, \tag{13}$$

$$(p_{i,j}^n - p_{cav;i,j}^n)(1 - \theta_{i,j}^n) = 0, \tag{14}$$

where

$$C_{i,j}(\boldsymbol{p}^n, \boldsymbol{\theta}^n) = - a_{i,j}^{-0} p_{i-1,j}^n - a_{i,j}^{+0} p_{i+1,j}^n - a_{i,j}^{0+} p_{i,j+1}^n - a_{i,j}^{0-} p_{i,j-1}^n - e_{i,j}^{-0} \theta_{i-1,j}^n + f_{i,j}^n, \tag{15}$$

with

$$
\begin{aligned}
&a_{i,j}^{00} = s_{i+1,j}^n + s_{i-1,j}^n + (\Delta x_1/\Delta x_2)^2 \left(s_{i,j+1}^n + s_{i,j-1}^n \right), &&e_{i,j}^{00} = (S\Delta x_1 + 2\Delta t/\Delta x_1)\, h_{i,j}^n, \\
&a_{i,j}^{+0} = -s_{i+1,j}^n, &&a_{i,j}^{-0} = -s_{i-1,j}^n, \\
&a_{i,j}^{0-} = -(\Delta x_1/\Delta x_2)^2\, s_{i,j-1}^n, &&a_{i,j}^{0+} = -(\Delta x_1/\Delta x_2)^2\, s_{i,j+1}^n, \\
&e_{i,j}^{-0} = -S\Delta x_1\, h_{i-1,j}^n, &&s_{i\pm1,j\pm1}^n = \frac{1}{6\mu}\left((h_{i,j}^n)^3 + (h_{i\pm1,j\pm1}^n)^3 \right). \\
&f_{i,j}^n = 2\Delta x_1/\Delta t\, h_{i,j}^{n-1}\theta_{i,j}^{n-1}
\end{aligned}
$$

Notice that $a_{i,j}^{00}, e_{i,j}^{00} \geq 0$, and each term $a_{i,j}^{+0}$, $a_{i,j}^{-0}$, $a_{i,j}^{0+}$, $a_{i,j}^{0-}$, $e_{i,j}^{-0}$ is non-positive, thus $C_{i,j}(\boldsymbol{p}^n, \boldsymbol{\theta}^n) \geq 0$. Alt (1980) studied this type of discrete system proposing a fixed-point method to solve it. Marini and Pietra (1986) also studied this system showing convergence of the resulting sequence to the solution of the discrete system when $T \equiv 0$.

3.1 Well posedness of the discrete system

Fixed-point framework. Let us omit the dependence of $C_{i,j}$ on the pair $(\boldsymbol{p}^n, \boldsymbol{\theta}^n)$ and the time step n in order to relax the notation. Following Alt (1980); Marini and Pietra (1986), the system

of equations (10)-(14) can be written as a fixed-point problem by defining the operator B_T as

$$(B_T(\boldsymbol{p}, \boldsymbol{\theta}))_{i,j} = \begin{cases} \left(\frac{1}{a_{i,j}^{00}} \left(C_{i,j} - e_{i,j}^{00} \right), 1 \right) & \text{if } C_{i,j} - e_{i,j}^{00} \geq a_{i,j}^{00} (T\boldsymbol{\theta})_{i,j} \\ \left((T\boldsymbol{\theta})_{i,j}, \frac{1}{e_{i,j}^{00}} \left(C_{i,j} - a_{i,j}^{00} (T\boldsymbol{\theta})_{i,j} \right) \right) & \text{if } C_{i,j} - e_{i,j}^{00} < a_{i,j}^{00} (T\boldsymbol{\theta})_{i,j} \end{cases},$$

for each cell $(i, j) \in I$. This way, Eq. (10) can be rewritten as the next fixed point problem

$$B_T(\boldsymbol{p}, \boldsymbol{\theta}) = (\boldsymbol{p}, \boldsymbol{\theta}). \tag{16}$$

Let us split the set I as $I = I_0 \overset{\circ}{\cup} I_r$, where I_r is the subset of cells in the region Λ_r^t and $I_0 = I \setminus I_r$. Please observe that a solution of Eq. (16) accomplishes automatically the conditions (11), (12) and (14) for any $(i, j) \in I$. However, the only immediate condition accomplished by $\theta_{i,j}$ is that $\theta_{i,j} \leq 1$. Now, please observe that

$$C_{i,j}(\boldsymbol{p}, \boldsymbol{\theta}) - a_{i,j}^{00}(T\boldsymbol{\theta})_{i,j} = f_{i,j} + S\Delta x_1 h_{i-1,j}\theta_{i-1,j} + \Delta_{i,j}'',$$

where

$$\Delta_{i,j}'' = s_{i-1,j} \left(p_{i-1,j} - (T\boldsymbol{\theta})_{i,j} \right) + s_{i+1,j} \left(p_{i+1,j} - (T\boldsymbol{\theta})_{i,j} \right) +$$
$$+ q^2 \left\{ s_{i,j-1} \left(p_{i,j-1} - (T\boldsymbol{\theta})_{i,j} \right) + s_{i,j+1} \left(p_{i,j+1} - (T\boldsymbol{\theta})_{i,j} \right) \right\}.$$

Thus, $\theta_{i,j}$ may be negative only on the cells in I_r such that some of its neighbors belongs to the set I_0. To overcome this issue the discrete version of the operator T is defined as follows

$$(T\boldsymbol{\theta})_{i,j} = \begin{cases} p_{cc}(t) & \text{if } (i, j) \in I_r \cup \partial I_r \\ 0 & \text{if } (i, j) \in I_0 \setminus \partial I_r \end{cases}, \tag{17}$$

where $\partial I_r = \{(i, j) \in I_0 : V(i, j) \cap I_r \neq \emptyset\}$ and $V(i, j) = \{(i \pm 1, j), (i, j \pm 1)\}$ (horizontal and vertical neighbors of (i, j)). Figure 3 illustrates the action of the discrete operator T.
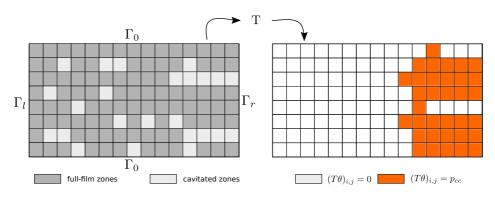

Figure 3: Illustration of the action of the discrete operator T. Notice that $(T\theta)_{i,j} = p_{cc}$ also on the neighbors of I_r.

Well-posedness. We define the iterative process

$$\left(\boldsymbol{p}^{k+1}, \boldsymbol{\theta}^{k+1} \right) = B_T \left(\boldsymbol{p}^k, \boldsymbol{\theta}^k \right), \tag{18}$$

starting from some initial guess $(\boldsymbol{p}^0, \boldsymbol{\theta}^0)$. The convergence of the sequence defined by Eq. (18) to a solution of equation (16) is proved by Marini and Pietra (1986) based in the monotonicity

of the operator B_0 (i.e., if $(\boldsymbol{p}_1, \boldsymbol{\theta}_1) \geq (\boldsymbol{p}_2, \boldsymbol{\theta}_2)$, by components, then $B_0(\boldsymbol{p}_1, \boldsymbol{\theta}_1) \geq B_0(\boldsymbol{p}_2, \boldsymbol{\theta}_2)$). On the other hand, for the operator T defined in (8), let us take some vector $\boldsymbol{p}$ and two vectors $\boldsymbol{\theta}_1, \boldsymbol{\theta}_2$, with $\boldsymbol{\theta}_1 > \boldsymbol{\theta}_2$, then, it can be seen that $(B_0(\boldsymbol{p}, \boldsymbol{\theta}_1))_{i,j} \geq (B_0(\boldsymbol{p}, \boldsymbol{\theta}_2))_{i,j}$ on the cells where $C_{i,j}(\boldsymbol{p}, \boldsymbol{\theta}_1) - e_{i,j}^{00} \geq a_{i,j}^{00}(T\boldsymbol{\theta}_1)_{i,j}$. However, on the cells where $C_{i,j}(\boldsymbol{p}, \boldsymbol{\theta}_1) - e_{i,j}^{00} < a_{i,j}^{00}(T\boldsymbol{\theta}_1)_{i,j}$ nothing can be assured, in fact, simple examples can be constructed where $(B_0(\boldsymbol{p}, \boldsymbol{\theta}_1))_{i,j} < (B_0(\boldsymbol{p}, \boldsymbol{\theta}_2))_{i,j}$ on those cells. Thus, for the operator T defined here the monotonicity is lost, and so the study the well-posedness of the discrete system is harder and left for future work.

4 NUMERICAL EXPERIMENTS

The algorithm used in this work for the numerical tests is shown in Table 1. It consists in a natural extension of the algorithm proposed by Marini and Pietra (1986). The upper surface is considered at rest while the lower moves to the right with velocity $U = 10$ m/s.

Table 1: Adaptation of the numerical algorithm presented in Marini and Pietra (1986) for the non-trivial operator T.

Algorithm 1: Numerical algorithm for solving the system (10)-(14).

Input: h: gap function, p^0, θ^0: initial guess
begin
  $k = 1$;
  $p^1 = p^0; \theta^1 = \theta^0$;
  while *change > tol* **do**
    compute $p_{cav}^k = T(\theta^k)$;
    for $i = 1 \ldots N_{x_1}, j = 1 \ldots N_{x_2}$ **do**
      if $\left(C_{i,j} - e_{i,j}^{00}\right)/a_{i,j}^{00} \geq p_{cav;i,j}^k$ **then**
        $p_{i,j}^k = (C_{i,j} - e_{i,j}^{00})/a_{i,j}^{00}$;
        $\theta_{i,j}^k = 1$;
      else
        $\theta_{i,j}^k = (C_{i,j} - a_{i,j}^{00}p_{cav;i,j}^k)/e_{i,j}^{00}$;
        $p_{i,j}^k = p_{cav;i,j}^k$;
      end
    end
    update arrays a and e;
  end
  compute $change = \|p^k - p^{k-1}\| + \|\theta^k - \theta^{k-1}\|$;
  $p^{k+1} = p^k; \theta^{k+1} = \theta^k$;
  $k = k + 1$;
  end
  return $p^{k+1}, \theta^{k+1}, p_{cav}^{k+1} \equiv T(\theta^{k+1})$;
end

For all cases the length of the pad along the x_1-axis is fixed as $L = 1$ mm, and the viscosity of the lubricant oil is set to $\mu = 4 \times 10^{-3}$ Pa·s.

4.1 Test 1: blow-by for a circular-shaped stationary ring

Due to the positive mechanical pressure at the combustion chamber, leaks of oil/gas through the ring-liner gap would occur, which is an undesirable effect known as *blow-by* (Wang and Chung, 2013). Here wee seek for some blow-by limit condition under the extended Elrod-Adams model. For this, we solve stationary cases taking a fixed value for p_{cc} with the next geometry

$$h(x_1) = \left(h_0 + \frac{(x_1 - 0.5 \times 10^{-3}[m])^2}{2R} \right) [\mu m].$$

After integration, the stationary Reynolds equation reads

$$\frac{\partial p}{\partial x_1} = 6\mu\, U \frac{(h - C)}{h^3}, \text{ on } [0, \beta], \tag{19}$$

where $0 < \beta < L$ corresponds to the oil film separation point and C is a constant equal to the mass-flux. The problem is closed imposing mass-conservation at $x_1 = \beta$ and the conditions:

$$p(0) = (1 - \chi)\, p_{cc}, \qquad p(\beta) = \chi\, p_{cc}, \qquad p(x_1) = \chi\, p_{cc}\, \forall x_1 \in\,]\beta, L], \tag{20}$$

$$\left. \frac{\partial p}{\partial x_1} \right|_{x_1 = \beta} \geq 0, \tag{21}$$

where $\chi \in \{0, 1\}$ is used to set the side where p_{cc} is imposed. Let us remember that the condition for the gradient at the separation point comes from imposing continuity of the flux function on $x_1 = \beta$, i.e.,

$$\left. \frac{U}{2} h\theta \right|_{+} - \left. \frac{h^3}{12\mu} \partial_{x_1} p \right|_{+} - \left. \frac{U}{2} h\theta \right|_{-} + \left. \frac{h^3}{12\mu} \partial_{x_1} p \right|_{-} = 0, \tag{22}$$

where the subscripts indicate right (+) or left (-) limits at β. Imposing also the continuity of the Couette term we get $\partial_{x_1} p|_{\beta_-} = 0$.

4.1.1 Case $\chi = 0$

We set $p(0) = p_{cc}$ and $p(L) = 0$. For these cases, whenever β exists, the pressure field accomplishes $p(x_1) \geq p(\beta)\, \forall x_1 \in [0, L]$. Thus, the restriction (21) turns to be $\partial_{x_1} p|_{\beta} = 0$ and, after integration, the solution is given by

$$p(x_1) = p_{cc} + 6\mu\, U \int_0^{x_1} \frac{h(s) - h(\beta)}{h(s)^3} ds, \tag{23}$$

$$p(\beta) = 0, \tag{24}$$

$$p(x_1) = 0, \qquad \forall x_1 \in\,]\beta, L]. \tag{25}$$

Please observe that when p_{cc} increases so does β. So the effect of a positive p_{cc} is to augment the mass-flux (which is constant through the domain). If p_{cc} is high enough, there is no β such that the first two equations are satisfied. In fact, this occurs when

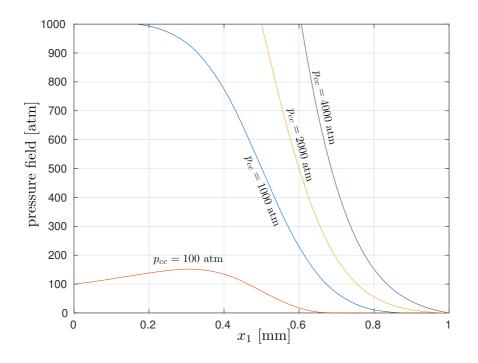$$p_{cc} > -6\mu\, U \int_0^L \frac{h(s) - h(L)}{h(s)^3} ds. \tag{26}$$

Figure 4: Example of solutions for case $\chi = 0$ with $R = 64$ mm and $h_0 = 1$ μm.

In such cases there is no condition on the gradient. However, there is no cavitation and we can just use the condition $p(L) = 0$ and integrate to obtain

$$p(x_1) = p_{cc} + 6\mu \int_0^{x_1} \frac{U\,h(s) - 2C}{h(s)^3} ds,\qquad(27)$$

where C is the mass-flux and must accomplish

$$p_{cc} = -6\mu \int_0^L \frac{U\,h(s) - 2C}{h(s)^3} ds.$$

We can notice that, when $\chi = 0$, p_{cc} can be as high as desired. An example of these solutions is showed in Fig. 4 for $R = 64$ mm, $h_0 = 1$ μm and different values of p_{cc}.

4.1.2   Case $\chi = 1$

First, we restrict the separation point β to be in $[L/2, L]$. With this, there exists some $\epsilon > 0$ such that $p(x_1) \geq p(\beta)$ for all $x_1 \in [\beta - \epsilon, \beta]$. Thus, we also recover the condition $\partial_{x_1} p|_\beta = 0$ and so Eq. (19) reads

$$\frac{\partial p}{\partial x_1}(x_1) = 6\mu\,U\,\frac{h(x_1) - h(\beta)}{h(x_1)^3}, \text{ on } [0, \beta].\qquad(28)$$

Integrating we obtain the next semi-analytic solution:

$$p(x_1) = 6\mu\,U \int_0^{x_1} \frac{h(s) - h(\beta)}{h(s)^3} ds,\qquad(29)$$

$$p(\beta) = p_{cc},\qquad(30)$$

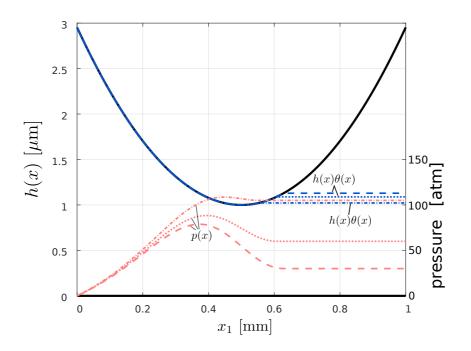$$p(x_1) = p_{cc}\,\forall x_1 \in\,]\beta, L].$$

Figure 5: Example of solutions for case $\chi = 1$. The dashed lines, dotted lines and dotted-dashed lines correspond to $p_{cc} = 30$, 60, and 105 atm respectively. $h\theta$ is the fluid height at each point.

where the second equation is solved numerically.

From equations (29) and (30) we observe that β diminishes as p_{cc} augments. As the mass-flux is equal to $C = \frac{U}{2}h(\beta)$, we see that C also diminishes when p_{cc} augments. Thus, with the restriction $\beta \in [L/2, L]$, the maximum value of p_{cc}, denoted p_{cc}^*, is

$$p_{cc}^* = 6\mu U \int_0^{L/2} \frac{h(s) - h(L/2)}{h(s)^3} ds. \tag{31}$$

As an example. Figure 5 shows the resulting pressure fields for $\chi = 1$, $h_0 = 1$ μm, $R = 64$ mm, $p_{cc} = 30$, 60, and 105 atm.

Lost of existence for $p_{cc} > p_{cc}^*$

If we suppose that for some $p_{cc} > p_{cc}^*$ there exists a separation point $0 < \beta < L/2$, then the mass-flux should be equal to

$$C = \frac{U}{2}h(\beta)\theta_+ = \frac{U}{2}h(\beta),$$

where we used the continuity of the Couette term. On the other hand, the flux at $x_1 = L/2$ would be equal to $\frac{U}{2}h(L/2) < C = \frac{U}{2}h(\beta)$, which is not possible since the mass-flux must be continuous. Thus, we can only have $\beta = L/2$, which also is not possible since the only possibility to accommodate a pressure $p(\beta = L/2)$ higher than p_{cc}^* is to admit a positive gradient pressure at the left side of β, but continuity of the Couette term implies a zero-gradient condition. This issue might be overcome allowing the Couette term to be discontinuous, which is left for further research.
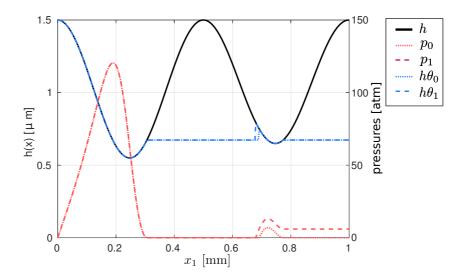
Figure 6: Resulting fields for Test 2. p_0 is the resulting pressure for $p_{cc} = 0$ atm and p_1 is the resulting pressure for $p_{cc} = 6$ atm. $h\theta$ is the fluid height at each point.

4.2 Test 2: two-cavitated areas at different cavitation pressure

For this stationary case the geometry is set as

$$h(x_1) = h_0 + \left[0.5(10^{-3}[m] - x_1) + 0.4\,x_1\right] \times 10^{-3}\cos(4\pi\,x_1 \times 10^3[m^{-1}]) + 1\,x_1 \times 10^{-4}),$$

where $h_0 = 1[\mu m]$ along with the inlet condition $\theta_\ell = 1$ (fully-flooded condition). The results for this case are shown in Fig. 6, where p_0 is the resulting pressure for $p_{cc} = 0$ atm and p_1 is the resulting pressure for $p_{cc} = 6$ atm. Focusing on p_1, please observe that two partial-film zones (i.e., $\theta < 1$) are formed, one near the center of the domain with cavitation pressure equal to 0 atm, and a second region where the cavitation pressure is equal to 6 atm. On the left pressurized region both p_0 and p_1 are equal, while on the right region p_1 is higher than p_0 due to the higher boundary condition. As a consequence, the hydrodynamical force (pressure integral) for $p_{cc} = 6$ atm is 10% higher than for $p_{cc} = 0$ atm.

4.3 Test 3: dynamic of a ring

In this case, the gap between the two surfaces reads

$$h(x_1, t) = Z(t) + h_p(x_1) = Z(t) + \frac{(x_1 - 0.5 \times 10^{-3}[m])^2}{2R}, \tag{32}$$

where the minimum clearance $Z(t)$ is found by solving the newton equation for the ring (extending Algorithm 1 by means of a Newmark scheme, as done by Ausas et al. (2009)), which is supposed to have a mass density of $m = 48 \times 10^{-3}$ kg/m and a curvature equal to $R = 64$ mm.
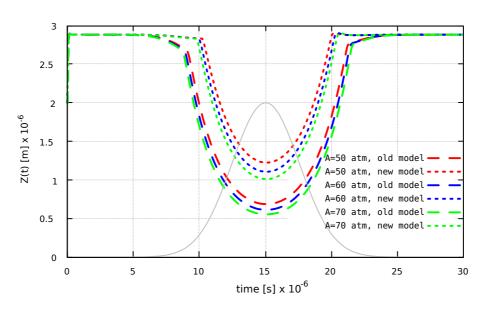
The forces acting on the ring along the x_3-axis are listed next

- $\boldsymbol{W^{ps}}$: the pre-stress elastic response to deformation (here taken equal to 40 N/m);

- $\boldsymbol{W^{gp}}$, the gas-pressure force originated from the leakage of the chamber pressure ($p_{cc}(t)$) through the gap that exists between the ring and the piston, modeled by (here we take $\gamma = 0.9$)

$$W^{gp}(t) = -\gamma\,p_{cc}(t);$$

- $\boldsymbol{W^h}$: the force originated from the hydrodynamical pressure $p(x_1, x_2, t)$ that develops in the oil film between the ring and the cylinder, given by $W^h = \int_\alpha^\beta p \, dx_1$, where $[\alpha, \beta] \subset [0, 1]$ is the region where the fluid is not *separated* from the ring. Notice that inside $[\alpha, \beta]$ cavitated regions ($0 \le \theta < 1$) could develop;

- $\boldsymbol{W^m}$: the force developed due to the mechanical pressure of the chamber under the ring, computed as $W^m = \int_\beta^1 p_{cc} \, dx$.

Along the x_1-axis the friction force per unit width can be computed as (Checo et al., 2016)

$$F(t) = -\int_0^L \left(\frac{\mu U}{h} + \frac{h}{2} \frac{\partial p}{\partial x_1} - p \frac{\partial h}{\partial x_1} \right) dx_1 \tag{33}$$

Figure 7: Pad position $Z(t)$ versus time for several explosion amplitudes A. The results of the extended model are presented in pointed lines, while the results for the Elrod-Adams model are presented in dashed lines. The Gaussian-like curve represents the chamber pressure in time (suitably normalized).

In this case we address the effects that an explosion in the combustion chamber may have on the ring dynamics of a PRCL. Such explosion is modeled by a Gaussian pulse that reads

$$p_{cc}(t) = A \cdot \exp\left(-1.3 \times 10^5 [s^{-2}] \cdot \left(t - 15 \times 10^{-3}[s]\right)^2\right),$$

with a time duration of about 20 ms. The oil feeding condition for all these cases is a film thickness of $h\theta = 3 \ \mu$m, placed at $x = 0$ mm ($x = 1$ mm) when U is positive (negative).

First, we compare the results between the Elrod-Adams model and its extension here proposed. Figure 7 shows the ring position $Z(t)$ for several explosion amplitudes A. As it can be observed, Elrod-Adams model predicts a minimum clearance $\approx 44\%$ smaller than the predicted by its extended model, which leads to a difference of $\approx 50\%$ in friction force relative to the computed with the extended model (Equation 33). This happens due to a higher hydrodynamic force (W^h) when considering the extended model, which is consequence of the proper accommodation of the combustion chamber pressure at the boundary (see Fig. 6).

Changing the explosion side

In the cases presented above, the explosion takes place at the right side of the domain, side that corresponds to the region where the oil film is exiting. During the compression/explosion strokes of a combustion engine the velocity of the piston changes its sign as shown in Fig. 8 for a typical diesel engine at 2000 rpm.
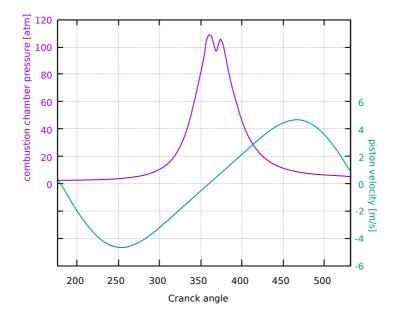

Figure 8: Typical piston velocity and combustion chamber pressure versus crank shaft angle at 2000 rpm.

To study the effects of this change of sign, we simulate again the cases exposed above but this time changing the explosion side, which is equivalent (for tribological measurements) to take $U = -10$ m/s. As can be observed in Fig. 9, when setting the explosion at the right side, the minimum clearance is $\approx 16\%$ bigger than when setting it at the left side, for each amplitude A tested.

To have a major insight on these results, we compute the solution in the stationary case. For this, we use the solutions found in Section 4.1 to compute the load-carrying capacity per unit width, which corresponds to the hydrodynamical force $W^h = \int_0^L p(x)\,dx$. Taking $p_{cc} = 3, 6, 12, 24$ and 48 atm, $h_0 = 0.25, 0.5, 1.0$ and 1.5 μm we compute $W^h_{\chi=0,\,h_0,\,p_{cc}}/W^h_{\chi=1,\,h_0,\,p_{cc}}$ and resume the results on Table 2. Please observe that for the range of values of p_{cc} and h_0 chosen, which is likely the range of values for the transitory cases shown in Fig. 9, it always happens that $W^h_{\chi=0,\,h_0,\,p_{cc}} \leq W^h_{\chi=1,\,h_0,\,p_{cc}}$. This explains why $Z(t)$ is always smaller when setting the explosion at the left side than when setting it at the right side.

h_0 [μm] \ p_{cc} [atm]	3	6	12	24	48
0.25	0.999	0.998	0.996	0.992	0.986
0.5	0.997	0.993	0.987	0.976	0.958
1.0	0.986	0.974	0.953	0.923	0.886
1.5	0.967	0.942	0.906	0.863	0.818

Table 2: $W^h_{\chi=0,\,h_0,\,p_{cc}}/W^h_{\chi=1,\,h_0,\,p_{cc}}$ for a range of h_0 and p_{cc}.
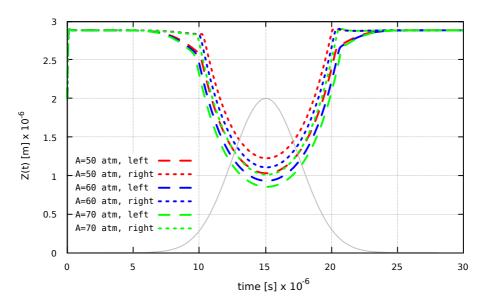
Figure 9: Pad position $Z(t)$ versus time for several explosion amplitudes A. The results of the extended model are presented in pointed lines, while the results for the Elrod-Adams model are presented in dashed lines. The Gaussian-like curve represents the chamber pressure in time (suitably normalized).

5 CONCLUSIONS AND FORTHCOMING RESEARCH

The proposed model attempts to include more appropriate boundary conditions when modeling the PRCL along the use of Reynolds equation along a mass-conservative extension of the Elrod-Adams model. This extension considers a dependence between the cavitation pressure and the saturation variable.

Numerical tests show that the proposed model predicts substantial differences in load-carrying capacity and friction as a result of a suitable accommodation of the combustion chamber pressure as a boundary condition.

Further research on the modeling of the operator T will be done. This, as to include interaction between partial-film areas cavitated at different pressures, which would allow to include texture on the liner surface. This inclusion is of great importance given the industrial interest on the direct simulation of the PRCL when including measured surface textures/roughness.

REFERENCES

Alt H.W. Numerical solution of steady-state porous flow free boundary problems. *Numer. Math.*, 36(1):73–98, 1980. ISSN 0029-599X. doi:10.1007/BF01395990.

Ausas R., Jai M., and Buscaglia G. A Mass-Conserving Algorithm for Dynamical Lubrication Problems With Cavitation. 131:031702 (7 pages), 2009.

Ausas R., Ragot P., Leiva J., Jai M., Bayada G., and Buscaglia G. The impact of the Cavitation model in the Analysis of Micro-Textured Lubricated Journal bearings. *ASME J. Tribol.*, 129(4):868–875, 2007.

Checo H.M., Ausas R., Jai M., Cadalen J., Choukroun F., and Buscaglia G.C. Moving textures:

Simulation of a ring sliding on a textured liner. *Tribol. Int.*, 72:131–142, 2014.

Checo H.M., Jaramillo A., Ausas R.F., and Buscaglia G.C. The lubrication approximation of the friction force for the simulation of measured surfaces. *Tribol. Int.*, 97:390–399, 2016. ISSN 0301679X. doi:10.1016/j.triboint.2015.12.030.

Dobrica M.B., Fillon M., Pascovici M.D., and Cicone T. Optimizing surface texture for hydrodynamic lubricated contacts using a mass-conserving numerical approach. *Proc. IMechE*, 224(8):737–750, 2010.

Etsion I. State of the art in laser surface texturing. *J. Tribol.: Trans. ASME*, 127:248–253, 2005.

Gadeschi G.B., Backhaus K., and Knoll G. Numerical Analysis of Laser-Textured Piston-Rings in the Hydrodynamic Lubrication Regime. *ASME J. Tribol.*, 134(4):1–8, 2012.

Kovalchenko A., Ajayi O., Erdemir A., Fenske G., and Etsion I. The Effect of Laser Texturing of Steel Surfaces and Speed-Load Parameters on the Transition of Lubrication Regime from Boundary to Hydrodynamic. *Tribol. T.*, 47(2):299–307, 2004. doi: 10.1080/05698190490440902.

Marini L.D. and Pietra P. Fixed-point algorithms for stationary flow in porous media. *Comput. Methods Appl. Mech. Eng.*, 56(1):17–45, 1986. ISSN 0045-7825. doi:10.1016/0045-7825(86)90134-9.

Morris N., Leighton M., De la Cruz M., Rahmani R., Rahnejat H., and Howell-Smith S. Combined numerical and experimental investigation of the micro-hydrodynamics of chevron-based textured patterns influencing conjunctional friction of sliding contacts. *Proc. Inst. Mech. Eng. Part J J. Eng. Tribol.*, (4), 2014. ISSN 1350-6501. doi:10.1177/1350650114559996.

Morris N., Rahmani R., Rahnejat H., King P.D., and Howell-Smith S. A Numerical Model to Study the Role of Surface Textures at Top Dead Center Reversal in the Piston Ring to Cylinder Liner Contact. *J. Tribol.*, 138(2):021703, 2015. ISSN 0742-4787. doi:10.1115/1.4031780.

Tomanik E. Friction and wear bench test of different engine liner surface finishes. *Tribol. Int.*, 41:1032–1038, 2008.

Usman A. and Park C.W. Optimizing the tribological performance of textured piston ring-liner contact for reduced frictional losses in SI engine: Warm operating conditions. *Tribol. Int.*, 99:224–236, 2016. ISSN 0301679X. doi:10.1016/j.triboint.2016.03.030.

Wang Q.J. and Chung Y.W. *Encyclopedia of Tribology*. Springer, first edition, 2013.